



Bergische Universität Wuppertal

Fakultät für Mathematik und Naturwissenschaften

Institute of Mathematical Modelling, Analysis and Computational
Mathematics (IMACM)

Preprint BUW-IMACM 25/14







Sergey Pereselkov, Venedikt Kuz'kin, Matthias Ehrhardt, Sergey Tkachenko,
Alexey Pereselkov and Nikolay Ladykin

Application of the Fractional Fourier Transform to Hologram Formation of a Moving Acoustic Source

September 6, 2025

<http://www.imacm.uni-wuppertal.de>

Application of the Fractional Fourier Transform to Hologram Formation of a Moving Acoustic Source

Sergey Pereselkov^{1,*}, Venedikt Kuz'kin², Matthias Ehrhardt³, Sergey Tkachenko¹ and Alexey Pereselkov¹ and Nikolay Ladykin¹

¹ Voronezh State University, Mathematical Physics and Information Technology Department, 394018 Voronezh, Russia; tkachenko.edu@yandex.ru (S.T.); pereselkov.edu@yandex.ru (A.P.)

² Prokhorov General Physics Institute of the Russian Academy of Sciences, 119991, Moscow, Russia; kumiov@yandex.ru

³ University of Wuppertal, Chair of Applied and Computational Mathematics, Gaußstraße 20, 42119 Wuppertal, Germany; ehrhardt@uni-wuppertal.de

* Correspondence: pereselkov@yandex.ru

Abstract: This paper examines how the fractional Fourier transform (FrFT) can be used to form and analyze acoustic holograms produced by a moving, linear, frequency-modulated (LFM) source in a shallow-water waveguide. In these environments, the source sound field creates an interference pattern, referred to as a two-dimensional interferogram, which represents the distribution of acoustic intensity in the frequency-time domain. This interferogram consists of parallel interference fringes. Consequently, focal points are formed and aligned along a straight line in the source hologram, which is represented by the two-dimensional Fourier transform of the interferogram. We have developed a holographic method for constructing the interferogram of an LFM source signal and transforming it into a Fourier hologram based on FrFT in the presence of strong noise. A key finding of this study is that the FrFT-based holographic method enables localized focal regions to emerge from modal interference even under high-intensity noise conditions. The positions of these focal spots are directly related to the source parameters, enabling the estimation of key characteristics such as the distance and velocity of the LFM source. We analyzed the effectiveness of the FrFT-based holographic method through numerical experiments in the 100–150 Hz frequency band. The results demonstrate the method's high noise immunity for source localization in realistic shallow-water environments under strong noise.

Keywords: fractional Fourier transform; FrFT-based holographic method; interferogram; hologram; linear frequency-modulation; shallow water

1. Introduction

The mathematical theory of the *fractional Fourier transform* (FrFT) was first proposed in 1980 [1] and laid the theoretical foundation for its application in signal processing. Currently, the FrFT is an effective mathematical framework for processing various types of complex signals, as demonstrated in various studies [2–6]. Unlike traditional methods, FrFT enables the development of a broader set of tools for signal analysis, including those that do not conform to the assumptions of integer-order Fourier transform (FT) [7]. By introducing fractional parameters, FrFT-based methods extend the concept of the Fourier transform, providing a more generalized framework for the time-frequency analysis of signals. This deepens our understanding of the time-frequency structure of signals and creates new opportunities for designing more efficient signal processing algorithms in many areas of application. The FrFT has found applications in quantum mechanics [1,2], optics [8–11], acoustics [12,13] as well as in different signal processing tasks [14–26]. It can be interpreted as a rotation in the time-frequency plane (Almeida, 1994). In other words, the FrFT defines the structure of a signal in FrFT domain coordinates. In this context, the concept of frequency is extended to FrFT frequency. From this perspective, the FrFT can be regarded as the spectral representation of a signal in the FrFT

domain. Next, the FrFT can be interpreted as the decomposition of a signal into sets of linear frequency modulation (LFM) signals [3]. In this case, the matched-order FrFT spectrum of the signal is more localized than its spectral distribution in the conventional Fourier transform (FT) domain.

Often, it is necessary to analyze the temporal structure of a signal in accordance with its FrFT frequencies. To accomplish this, the signal must be represented in the joint time-FrFT frequency domain. This representation is called the *short-time fractional Fourier transform* (STFrFT), an analog of the short-time Fourier transform (STFT) [27–30]. This topic has been studied in [31–34]. The most efficient STFrFT-based signal processing method was proposed in [35]. The STFrFT signal processing method proposed in this work differs from the approaches in [31–34] in that it enables analysis of the two-dimensional (2D) signal structure in the time-frequency domain, i.e., the STFrFT domain. When the matched order of the STFrFT is selected, the chirp signal exhibits a compact localization region in the STFrFT domain. This indicates that the STFrFT plays an important role in two-dimensional signal processing. Furthermore, as demonstrated in [35], the STFrFT possesses rotational additivity, providing a horizontal orientation to the signal structure, which is advantageous for analyzing and processing chirp signals. The STFrFT method, as presented in [35], proves to be highly effective in suppressing noise in signals.

Advances in signal processing methods based on the Fourier transform (FrFT) have occurred simultaneously with the above-described developments. Significant progress has also been made in *interferometric signal processing* (ISP) for underwater acoustics. ISP is founded on analyzing stable interference structures in the time-frequency domain that arise during the propagation of broadband acoustic signals in shallow-water waveguides [36,37]. This makes the ISP approach conceptually similar to signal processing methods based on the FT and FrFT. Several seminal studies [38–40] provided comprehensive accounts of the theoretical underpinnings and methodological aspects of ISP. A diverse body of research has demonstrated the applicability of ISP across multiple practical domains. For instance, [41,42] used interferometric methods to estimate waveguide-invariant parameters. Another study illustrated the enhancement of weak signals when ISP is combined with array beamforming [43]. In [44], ISP techniques were used for seabed classification with ship-generated acoustic fields. Other contributions include developing a range-estimation algorithm for shallow-water environments [45] and an invariant-based method independent of source distance [46]. Additionally, [47] established a direct link between interference fringes and eigenray (or eigenbeam) arrival times.

The versatility of ISP has also been confirmed in deep-ocean scenarios, where it has been adapted for passive sonar applications [48,49]. One of the most advanced ISP-based methodologies in this context is *holographic signal processing* (HSP) [50–52]. The fundamental physical and mathematical principles governing hologram formation were first formulated in [51,52]. According to the HSP paradigm, quasi-coherent integration of acoustic intensity in the frequency-time domain produces an *interferogram* $I(\omega, t)$ [52]. To further interpret the accumulated intensity distribution, a two-dimensional Fourier transform is applied, yielding the so-called *Fourier hologram*: $F(\tau, \tilde{\nu}) = \mathcal{F}_{2D}\{I(\omega, t)\}$. This hologram representation $F(\tau, \tilde{\nu})$ concentrates the acoustic energy contained in $I(\omega, t)$ into localized focal regions that arise as a consequence of modes interference. The hologram $F(\tau, \tilde{\nu})$ exhibits a high focusing capability surpassing the performance of traditional focusing techniques. Such techniques include wavefront reversal or time reversal of the wave to the position of the primary source [53]. Unlike these approaches, the proposed method automatically localizes the two-dimensional source intensity directly at the receiver point, without the need for extended antenna arrays.

The papers [51,52], analyzed HSP for the low-frequency band for a regular waveguide. In paper [54], HSP was analyzed for the high-frequency band. The HSP method was analyzed for an irregular waveguide in the presence of internal waves [55,56] and in the presence of irregular bathymetry [57]. A review of the results obtained to date within the framework of the HSP method is presented in [58]. However, the potential of the HSP method for processing LFM signals [12] in the presence of noise [59,60] has not yet been explored. LFM signals are widely used in large-scale ocean field experiments. They are an effective tool for studying the oceanic environment and are used in many large-scale field

experiments [61–65]. This paper addresses this issue. The authors believe that applying the FrFT to the hologram formation of an LFM source yields stable results, even when the noise level significantly exceeds that of the signal.

This paper studies the application of the FrFT to the formation and analysis of acoustic holograms generated by a moving LFM signal source in a shallow-water waveguide. In these environments, the source sound field creates an interference pattern, known as a two-dimensional interferogram, which represents the distribution of acoustic intensity in the frequency-time domain. This interferogram consists of parallel interference fringes. Consequently, focal points are formed and aligned along a straight line in the source hologram, which is represented by the two-dimensional Fourier transform of the interferogram. A holographic method has been developed for constructing the interferogram of an LFM signal source and transforming it into a Fourier hologram based on the FrFT in the presence of strong noise. A key finding of this study is that the FrFT-based holographic method can produce localized focal regions resulting from modal interference, even in the presence of high-intensity noise. The positions of these focal spots are directly related to the source parameters, enabling the estimation of such key characteristics, such as the distance and velocity of the LFM signal source. The effectiveness of the FrFT-based holographic method has been analyzed through numerical experiments in the 100–150 Hz frequency band. The presented results demonstrate the method’s high immunity to noise for source localization in realistic, shallow-water environments with strong noise.

This paper is organized into five sections. Section 1 provides an introduction. Section 2 presents the theoretical foundations of holographic signal processing based on the FrFT, including the shallow-water waveguide model, the formulation of the LFM source signal, the waveguide’s transfer function, and the mathematical framework for interferogram and hologram formation. The use of STFrFT for analyzing and filtering chirp signals in the time-FrFT-frequency domain is emphasized. Section 3 describes the setup and results of the numerical simulations. It provides the acoustic parameters of the shallow-water environment and details the characteristics of the LFM signal used for the simulations. It also analyzes the structure of the received LFM signal for stationary and moving LFM sources under different noise conditions, including noise-free and with noise (SNR=–30 dB). The structures of the interferograms and holograms of the LFM source are also analyzed under various noise conditions. This section demonstrates that FrFT-based filtering enables the recovery of interferogram and hologram structures close to those obtained in the absence of noise, even under severe noise contamination. Estimates of key source parameters (range and velocity) are derived from the positions of the hologram’s focal spots for different noise conditions. A comparative analysis of these estimates demonstrates the effectiveness of FrFT-based holographic signal processing in shallow water. Section 4 concludes the study by summarizing the main findings and outlining potential directions. Section 5 describes the next phase of our research.

2. Holographic Signal Processing Based on Fractional Fourier Transform

This section presents an algorithm for constructing the hologram of a moving LFM signal source using on the FrFT. Section 2 consists of seven parts. The first part, Section 2.1, describes the shallow water waveguide model used in the paper. The shallow water waveguide transfer function is constructed within the framework of the modal description of the acoustic field in Section 2.2. Section 2.3 is devoted to describing of the LFM signal model emitted by the source. Section 2.4 presents a description of the LFM signal model as it propagates through the shallow water waveguide and is received by the receiver. Section 2.5 is devoted to applying the FrFT to process the LFM signal recorded by the receiver. Section 2.6 presents the interferogram of the signal obtained at the receiver. Section 2.7 provides a description of the signal hologram at the receiving point.

2.1. Shallow Water Waveguide Model

First, we describe the two-dimensional representation of the shallow-water waveguide used in our work (see Figure 1). The waveguide is formulated in the Cartesian coordinate system (r, z) and is characterized by the depth-dependent sound speed $c(z)$, refractive index $n(z)$, and density $\rho(z)$. The

water layer is bounded at the top by the free surface at $z = 0$ and at the bottom by the seabed located at $z = H$.

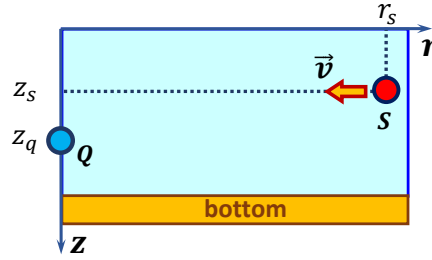


Figure 1. Shallow water waveguide model. Moving source and receiver.

The seabed is characterized by its density ρ_b and by the refractive index $n_b(1 + i\kappa)$ [66–68], where κ is the attenuation parameter expressed as $\kappa = \chi c_b / (54.6f)$. Here, χ stands for the bottom loss coefficient, c_b is the sound speed within the bottom medium, and f corresponds to the acoustic frequency.

2.2. Shallow Water Waveguide Transfer Function

Consider an underwater acoustic scenario in a shallow water waveguide (Figure 1). The receiver is positioned at point $Q(r_q, z_q)$, and the stationary source is assumed to be placed at the origin of the coordinate system ($r_q = 0$). A moving sound source is located at point $S(r_s, z_s)$, with its velocity denoted by \vec{v} . Under the assumptions of vertical modes and the approximation of horizontal rays, the transfer function $H(\omega, r_s)$ of the shallow water waveguide (see Section 2.1) can be written as follows, cf. [66–68]:

$$H(\omega, r_s) = \frac{ie^{-i\pi/4}}{\rho(z_s)\sqrt{8\pi}} \sum_{m=1}^M \frac{\phi_m(z_s, \omega) \phi_m(z_q, \omega)}{\sqrt{h_m}} \exp(ir_s h_m - r_s \gamma_m) \quad (1)$$

In this context, r_s represents the distance between the source and the receiver, and $\phi_m(z, \omega)$ corresponds to the vertical distribution (mode shape) of the m -th acoustic mode in the shallow-water waveguide. The complex horizontal wavenumber of a given mode is expressed as $\xi_m(\omega) = h_m(\omega) + i\gamma_m(\omega)$, where h_m and γ_m denote its real and imaginary components, respectively. The summation is carried out up to M , which is the total number of propagating modes in the shallow-water environment. The angular frequency is defined as $\omega = 2\pi f$. The mode functions $\phi_m(z, \omega)$ together with the complex wavenumbers ξ_m are determined by solving the corresponding *Sturm-Liouville eigenvalue problem* subject to the boundary conditions imposed by the free surface at the top and the seabed at the bottom, [66–68]:

$$\frac{d^2 \phi_m(\omega, z)}{dz^2} + k^2 n^2(z) \phi_m(\omega, z) = \xi_m^2 \phi_m(\omega, z), \quad (2)$$

$$\phi_m(\omega, z)|_{z=0} = 0, \quad \phi_m(\omega, z)|_{z=H} + g(\xi_m) \frac{d\phi_m(\omega, z)}{dz} \Big|_{z=H} = 0. \quad (3)$$

Here

$$g(\xi_m) = \eta / \sqrt{\xi_m^2 - k^2 n_b^2(1 + i\kappa)}, \quad k = \omega / c. \quad (4)$$

The mode functions $\phi_m(\omega, z)$ satisfy the following orthonormality condition:

$$\int_0^H \phi_l \phi_m dz + \eta \int_H^\infty \phi_l \phi_m dz = \delta_{ml}, \quad (5)$$

where δ_{ml} denotes the Kronecker delta.

Hereafter, the transfer function of the waveguide will be denoted as $H(\omega, r_s) = H(\omega)$.

2.3. Source LFM Signal

Consider the LFM source signal at the emission point. An LFM signal is a type of waveform whose instantaneous frequency changes linearly with time and is also commonly referred to as a *chirp signal*. LFM signals are widely used in large-scale ocean acoustic experiments in underwater acoustics. They are an efficient tool for investigating the marine environment and have been used in many field campaigns [61–65].

2.3.1. Time Domain

The time instantaneous frequency of an LFM signal sweeping from a starting frequency f_1 to an ending frequency f_2 over a time interval τ is given by

$$f(t) = f_1 + \frac{(f_2 - f_1)}{\tau} t, \quad 0 \leq t \leq \tau. \quad (6)$$

The time instantaneous phase $\varphi(t)$ of the signal can be obtained by integrating the instantaneous angular frequency $\omega(t) = 2\pi f(t)$:

$$\varphi(t) = \begin{cases} 2\pi \left(f_1 t + \frac{f_2 - f_1}{2\tau} t^2 \right), & 0 \leq t \leq \tau, \\ 0, & t > \tau. \end{cases} \quad (7)$$

The instantaneous LFM signal in the time domain is expressed as

$$s(t) = \begin{cases} A \cos \left(2\pi f_1 t + \pi \frac{f_2 - f_1}{\tau} t^2 \right), & 0 \leq t \leq \tau, \\ 0, & t > \tau. \end{cases} \quad (8)$$

2.3.2. Frequency Domain

The instantaneous LFM signal in the frequency domain derived by the FT of $s(t)$ is

$$S(\omega) = \int_0^\infty s(t) e^{-i\omega t} dt. \quad (9)$$

This integral corresponds to a Fresnel-type integral. Its approximate closed-form solution yields the complex spectrum as

$$S(\omega) = \begin{cases} A \sqrt{\frac{\tau}{|f_2 - f_1|}} \exp \left[-i \frac{(\omega - 2\pi f_0)^2 \tau}{4\pi(f_2 - f_1)} \right], & \omega \in [2\pi f_1, 2\pi f_2], \\ 0, & \omega \notin [2\pi f_1, 2\pi f_2]. \end{cases} \quad (10)$$

The magnitude spectrum $|S(\omega)|$ therefore has the form

$$|S(\omega)| \approx \begin{cases} A \sqrt{\frac{\tau}{|f_2 - f_1|}}, & \omega \in [2\pi f_1, 2\pi f_2], \\ 0, & \omega \notin [2\pi f_1, 2\pi f_2]. \end{cases} \quad (11)$$

The phase of the complex spectrum $\arg(S(\omega))$ has the form:

$$\arg\{S(\omega)\} \approx \begin{cases} -\frac{\tau}{4\pi(f_2 - f_1)} (\omega - 2\pi f_0)^2, & \omega \in [2\pi f_1, 2\pi f_2], \\ 0, & \omega \notin [2\pi f_1, 2\pi f_2]. \end{cases} \quad (12)$$

2.3.3. Parameters of LFM Signal

- f_1 is the initial frequency at $t = 0$,
- f_2 is the final frequency at $t = \tau$,
- $f_0 = (f_1 + f_2)/2$ is the central frequency,

- τ is the duration of the frequency sweep,
- $\Delta f = f_2 - f_1$ is frequency bandwidth,
- LFM is called an *up-chirp* if $f_2 > f_1$,
- LFM is called a *down-chirp* if $f_2 < f_1$,
- A is the signal amplitude.

Hereafter, the source signal will be denoted as $s_s(t)$ in the time domain and as $S_s(\omega)$ in the frequency domain.

2.4. Receiver LFM Signal

Now, let us examine the acoustic signal observed at the receiver location. Let $S_r(\omega)$ be the spectrum of the received waveform. When the transmitted signal propagates through a shallow water waveguide, the medium can be modeled as a linear, time-invariant system characterized by its transfer function $H(\omega)$ (Equation (1)). Under this assumption, the received spectrum is obtained as the product of the transmitted spectrum $S_s(\omega)$ (Equation (10)) and the transfer function $H(\omega)$ of the propagation channel, namely

$$S_r(\omega) = S_s(\omega) H(\omega). \quad (13)$$

This relation emphasizes that the spectral content of the received signal is shaped by the properties of the source waveform and the frequency-dependent response of the shallow water waveguide.

Assuming that the source signal is an LFM waveform, it sweeps continuously from the initial frequency f_1 to the final frequency f_2 within the duration of the emission interval τ . As a result, we obtain the following expression for the spectrum of the received signal

$$S_r(\omega) = \begin{cases} H(\omega) A \sqrt{\frac{\tau}{|f_2 - f_1|}} \exp \left[-i \frac{(\omega - 2\pi f_0)^2 \tau}{4\pi(f_2 - f_1)} \right], & \omega \in [2\pi f_1, 2\pi f_2], \\ 0, & \omega \notin [2\pi f_1, 2\pi f_2]. \end{cases} \quad (14)$$

The magnitude spectrum $|S(\omega)|$ therefore has the form

$$|S_r(\omega)| \approx \begin{cases} |H(\omega)| A \sqrt{\frac{\tau}{|f_2 - f_1|}}, & \omega \in [2\pi f_1, 2\pi f_2], \\ 0, & \omega \notin [2\pi f_1, 2\pi f_2]. \end{cases} \quad (15)$$

The phase of the complex spectrum $\arg(S(\omega))$ has the form

$$\arg\{S_r(\omega)\} \approx \begin{cases} \arg\{H(\omega)\} - \frac{\tau}{4\pi(f_2 - f_1)} (\omega - 2\pi f_0)^2, & \omega \in [2\pi f_1, 2\pi f_2], \\ 0, & \omega \notin [2\pi f_1, 2\pi f_2]. \end{cases} \quad (16)$$

The LFM signal's wide bandwidth ($[f_1, f_2]$) allows its interaction with the shallow-water waveguide to be described in terms of amplitude and phase distortions introduced by the channel. At the receiver, the chirp's overall spectral extent remains essentially unchanged: the signal's frequency content still occupies the interval $[f_1, f_2]$, and no additional frequencies are generated outside this band. However, the propagation medium selectively modifies the relative amplitudes and phases of the individual harmonic components within this spectral range. Specifically, the amplitude response $|H(\omega)|$ does not remove frequencies from the interval $[f_1, f_2]$ but rather introduces frequency-dependent attenuation that reshapes the spectral envelope. Consequently, while the useful chirp bandwidth is preserved in a nominal sense, the relative energy distribution across the band may no longer be uniform. This reduces the effective resolution attainable after matched filtering. Similarly, the phase response $\arg H(\omega)$ alters the phase relationships among the spectral components. This corresponds to frequency-dependent group delays, meaning that different portions of the chirp spectrum arrive at the receiver with varying temporal offsets. For an LFM signal, this effect manifests itself as a nonlinear distortion of the instantaneous frequency law $f(t)$, leading to temporal dispersion, pulse broadening,

and a departure from the ideal linear chirp structure. These amplitude and phase effects preserve the nominal spectral support of the transmitted waveform while significantly modifying the detailed structure of the received spectrum inside the interval $[f_1, f_2]$.

2.5. Fractional Fourier Transform

Next, let us review the background of the FrFT in holographic signal processing.

2.5.1. Fractional Fourier Transform

The $S_p(u)$ is the FrFT of the signal $s(t)$ and can be expressed by the following way [31–33,35?]

$$S_p(u) = \mathcal{F}^p\{s(t)\} = \int_{-\infty}^{+\infty} s(t) K_p(t, u) dt \quad (17)$$

where $K_p(t, u)$ is the kernel function of the FrFT, $p = \frac{2\alpha}{\pi}$ is the order of the FrFT, and α is the rotation angle of the u -axis in the FrFT domain.

The FrFT kernel function $K_p(t, u)$ is expressed as follows

$$K_p(t, u) = \begin{cases} \sqrt{\frac{1-i\cot\alpha}{2\pi}} \exp\left(i\frac{t^2+u^2}{2} \cot\alpha - itu \csc\alpha\right), & \alpha \neq k\pi, \\ \delta(u - t), & \alpha = 2k\pi, \\ \delta(u + t), & \alpha = (2k + 1)\pi, \end{cases} \quad (18)$$

where $\delta(u)$ denotes the Dirac delta function. The inverse FrFT provides a way to reconstruct the original signal $s(t)$ from its known transformed representation $S_p(u)$:

$$s(t) = \int_{-\infty}^{+\infty} S_p(u) K_p^*(t, u) du. \quad (19)$$

2.5.2. Short Time Fractional Fourier Transform

Consider the short-time extension of the fractional Fourier transform (STFrFT) [35]. Unlike conventional approaches, the STFrFT represents both temporal and FrFT frequency information simultaneously on the joint time-FrFT frequency plane. This provides the signal with a two-dimensional support region. When performed with the appropriate fractional order, the transform yields a compact support region for chirp signals in this domain, demonstrating the STFrFT's effectiveness in holographic signal processing. Furthermore, the STFrFT preserves the additivity property of rotation and yields a horizontally oriented support region for LFM signals, significantly facilitating their analysis and processing. For example, the STFrFT is an effective tool for suppressing noise and enhancing the clarity of LFM signals in holographic signal processing.

The STFrFT is obtained by multiplying the signal by a window function before applying the FrFT:

$$S_p(t, u) = \int_{-\infty}^{+\infty} s(\tau) w(\tau - t) K_p(\tau, u) d\tau. \quad (20)$$

where $w(t)$ is the window function. The efficiency of an STFrFT at a given order depends on both the form and duration of the window. In [?], the optimal window function was analyzed. Two main conditions are typically applied when selecting an appropriate window function: (1) achieving high 2D resolution, and (2) ensuring a compact STFrFD support region of the signal. Therefore, the optimal window function provides the STFrFT with maximum 2-D resolution while keeping the support region as small as possible. A Gaussian window function leads to the maximum 2D resolution. For convenience, consider a unit-energy Gaussian window:

$$w(t) = (\pi \sigma^2)^{-1/4} e^{-t^2/(2\sigma^2)}, \quad (21)$$

where σ is the width of the window function. 247

The inverse short-time fractional Fourier transform enables us to reconstruct the original signal $s(t)$ from its transformed form $S_p(u)$: 248

$$x(\rho) = \int_{-\infty}^{+\infty} \int_{-\infty}^{+\infty} S_p(t, u) w(\rho - t) K_{-p}(\rho, u) dt du. \quad (22) \quad 249$$

Here, $K_{-p}(t, u)$ is the kernel function of the inverse FrFT: 250

$$K_{-p}(t, u) = K_p^*(t, u). \quad (23) \quad 251$$

In summary, the STFrFT provides a powerful framework for holographic signal processing. It enables the denoising and reconstruction of LFM signals with enhanced time-frequency resolution and robustness against noise. 252

- The FrFT is equivalent to a rotation in the time-frequency plane. For an LFM signal, this rotation transforms an oblique spectral line into a vertical concentration, thereby maximizing energy compaction. 253
- The STFrFT inherits the localization properties of the short-time transform, enabling joint (t, u) analysis and effective denoising. 254

2.6. Interferogram of LFM Signal 255

In this section, we analyze the interferogram produced by a moving acoustic source. The distance between the source and the receiver varies over time and can be expressed as follows 256

$$r(t) = r_0 - vt, \quad (24) \quad 257$$

where r_0 is the initial position of the source at $t_0 = 0$, t is the current observation time, and v denotes the constant velocity of the moving source. 258

The two-dimensional interferogram $I(\omega, t)$ describes the distribution of the received acoustic intensity in the joint frequency-time domain (ω, t) and is initially expressed as 259

$$I(\omega, t) = |S_r(\omega, t)|^2. \quad (25) \quad 260$$

According to Eq. (13), this representation can be further written in terms of the power spectrum of the transmitted waveform and the channel response: 261

$$I(\omega, t) = |S_s(\omega)|^2 |H(\omega, t)|^2. \quad (26) \quad 262$$

In turn, the transfer function of the shallow-water waveguide $H(\omega, t)$ is expressed, following Eq. (1), in terms of the normal modes of the environment: 263

$$H(\omega, t) = \sum_{m=1}^M H_m(\omega, t) \exp\{ih_m(r_0 - vt)\}, \quad (27) \quad 264$$

where the individual mode contribution $H_m(\omega, t)$ is defined as 265

$$H_m(\omega, t) = \frac{ie^{-i\pi/4}}{\rho(z_s)\sqrt{8\pi}} \frac{\phi_m(z_s, \omega) \phi_m(z_q, \omega)}{\sqrt{h_m}} \exp\{-\gamma_m(r_0 - vt)\}. \quad (28) \quad 266$$

Here $\phi_m(z, \omega)$ are the mode eigenfunctions, h_m and γ_m represent the real and imaginary parts of the modal horizontal wavenumber, respectively, and $\rho(z_s)$ is the density at the source depth. 267

As a result, the interferogram $I(\omega, t)$ of the moving source in the frequency-time domain can be expressed as the coherent superposition of cross-terms between different modes:

$$\begin{aligned} I(\omega, t) &= |S_s(\omega)|^2 \sum_m \sum_n H_m(\omega, t) H_n^*(\omega, t) \exp[ih_{mn}(\omega)(r_0 - vt)] \\ &= \sum_m \sum_n I_{mn}(\omega, t), \quad m \neq n, \end{aligned} \quad (29)$$

where $h_{mn}(\omega) = h_m(\omega) - h_n(\omega)$ is the difference of the real parts of the modal horizontal wavenumbers. The term $I_{mn}(\omega, t)$ represents a partial interferogram that results from the interference between the m -th and n -th modes. The superscript $*$ denotes complex conjugation. The restriction $m \neq n$ indicates that the mean (auto-term) contribution has been excluded. Thus, $I(\omega, t)$ reflects only the modal interference structure.

2.7. Hologram of LFM Signal

This section focuses on the holographic representation of a moving source of LFM signals in a shallow water waveguide. To extract the holographic features from the measured acoustic field, we apply a two-dimensional Fourier transform (2D-FT) to the interferogram $I(\omega, t)$, which was introduced in Eq. (14). This transformation maps the signal from the frequency-time domain (ω, t) into the hologram domain $(\tau, \tilde{\nu})$, producing the function $F(\tau, \tilde{\nu})$ that can be written as

$$\begin{aligned} F(\tau, \tilde{\nu}) &= \sum_m \sum_n \int_0^{\Delta t} \int_{\omega_1}^{\omega_2} I_{mn}(\omega, t) \exp[i(\tilde{\nu}t - \omega\tau)] dt d\omega \\ &= \sum_m \sum_n F_{mn}(\tau, \tilde{\nu}), \end{aligned} \quad (30)$$

where τ is the time-lag variable, and $\tilde{\nu} = 2\pi\nu$ is the angular frequency in the hologram plane. Each term $F_{mn}(\tau, \tilde{\nu})$ corresponds to the interference contribution between the m -th and n -th acoustic modes. The integration over ω extends across the signal band, from $\omega_1 = \omega_0 - \Delta\omega/2$ to $\omega_2 = \omega_0 + \Delta\omega/2$, where $\Delta\omega$ is the bandwidth of the transmitted waveform, ω_0 is the central frequency, and Δt is the total observation time.

Assuming that the modal amplitudes and the spectral distribution of the field vary only slowly with frequency compared to the rapid oscillatory dependence of the phase term $\exp[ih_m(\omega)(r_0 - vt)]$, the partial hologram can be approximated by the simplified analytical form

$$\begin{aligned} F_{mn}(\tau, \tilde{\nu}) &= |S_s(\omega)|^2 H_m(\omega_0) H_n^*(\omega_0) \Delta\omega \Delta t \exp[i\Phi_{mn}(\tau, \tilde{\nu})] \times \\ &\quad \times \frac{\sin\left\{ \left[r_0 \frac{dh_{mn}(\omega_0)}{d\omega} - \tau \right] \frac{\Delta\omega}{2} \right\} \sin\left\{ [vh_{mn}(\omega_0) + \tilde{\nu}] \frac{\Delta t}{2} \right\}}{\left[r_0 \frac{dh_{mn}(\omega_0)}{d\omega} - \tau \right] \frac{\Delta\omega}{2} [vh_{mn}(\omega_0) + \tilde{\nu}] \frac{\Delta t}{2}}, \end{aligned} \quad (31)$$

with the phase of the partial hologram given by

$$\Phi_{mn}(\tau, \tilde{\nu}) = \left(\frac{\tilde{\nu}\Delta t}{2} - \tau\omega_0 \right) + h_{mn}(\omega_0) \left(\frac{\Delta t}{2} v + r_0 \right). \quad (32)$$

The location of the focal spot closest to the origin in the hologram plane yields direct estimates of the kinematic parameters of the moving source, namely, its radial velocity and initial position. Following [50–52], these estimates are obtained from

$$\dot{v} = -k_v \tilde{\nu}_1, \quad \dot{r}_0 = k_r \tau_1, \quad (33)$$

where the proportionality coefficients are defined as

$$k_v = (M - 1)(h_{1M}(\omega_0))^{-1}, \quad k_r = (M - 1) \left(\frac{dh_{1M}(\omega_0)}{d\omega} \right)^{-1}. \quad (34)$$

Here the overdot notation indicates that the values are not the exact source parameters, but rather their estimates obtained by means of holographic processing.

The holographic signal processing algorithm operates as follows. The spatial-spectral structure of the hologram $F(\tau, \tilde{\nu})$ is markedly different from that of the original interferogram $I(\omega, t)$, the relationship between them is strictly bijective. In other words, the hologram provides a complete and unique representation of the interferogram. Consequently, applying the inverse 2D Fourier transform to $F(\tau, \tilde{\nu})$ fully reconstructs the original interferogram $I(\omega, t)$, thus ensuring that no information about the propagation channel or modal interference pattern is lost.

3. Numerical Simulation Results

The Section 3 presents the configuration and outcomes of the numerical simulations. The acoustic parameters of the shallow-water environment are presented, and stationary and moving low-frequency modulation (LFM) sources are examined in the presence of noise. The analysis focuses on the structure of interferograms and holograms of an LFM signal in the presence of noise. It illustrates how the STFrFT can suppress noise and how the positions of focal spots can accurately estimate key source parameters, such as range and velocity, even in noisy environments. Particular emphasis is placed on applying the STFrFT to analyze and filter chirp signals in the time-FrFT-frequency domain.

Section 3 consists of five parts. The Section 3.1 provides a detailed description of the parameters of the transmitted LFM source signal, including the carrier frequency, bandwidth, duration, and modulation characteristics. These parameters form the basis for the simulation scenarios. Section 3.2 introduces the acoustic parameters of the shallow water waveguide and the waveguide transfer function. Section 3.3 defines the simulation framework for the received LFM signal in the presence of noise. The received signal spectrum is modeled as the product of the LFM source spectrum and the waveguide transfer function, plus a realization of the noise spectrum. Section 3.4 presents and analyzes the interferogram and hologram for a stationary LFM source. The focus is on using the SFrFT for noise suppression and forming focal spots, which enable the accurate estimation of stationary-source parameters in noisy environments. The feasibility of estimating these parameters under noisy conditions is demonstrated. Section 3.5 examines interferograms and holograms generated by a moving LFM source. The emphasis is on applying the SFrFT to suppress noise and on focal spot formation to accurately estimate the parameters of a moving source in a noisy environment. The motion-induced displacement of focal spots is analyzed, and the feasibility of estimating the parameters of a moving LFM source in a noisy environment is demonstrated.

3.1. Source LFM Signal Parameters

At the source, we consider an LFM (up-chirp) waveform. Its instantaneous frequency sweeps linearly over time (see Eqs. (6)–(8)). These signals are widely used in large-scale ocean acoustic experiments because they efficiently probe the marine environment. They have been used in numerous field campaigns [61–65].

Table 1 summarizes the parameters of the LFM source signal used in the numerical simulation.

Table 1. LFM source signal parameters.

Parameter	$\Delta f = 100\text{--}150\text{ Hz}$
1. Initial frequency at $t = 0$	100 Hz
2. Final frequency at $t = \tau$	150 Hz
3. Central frequency $f_0 = (f_1 + f_2)/2$	$f_0 = 125\text{ Hz}$
4. Duration of the frequency sweep	$\tau = 3\text{ s}$
5. Frequency bandwidth $\Delta f = f_2 - f_1$	$\Delta f = 50\text{ Hz}$
6. Slope $k = (f_2 - f_1)/\tau$	$k = 16.667\text{ Hz/s}$
7. LFM type signal	<i>up-chirp</i> : $f_2 > f_1$
8. Signal amplitude	$A = 1$

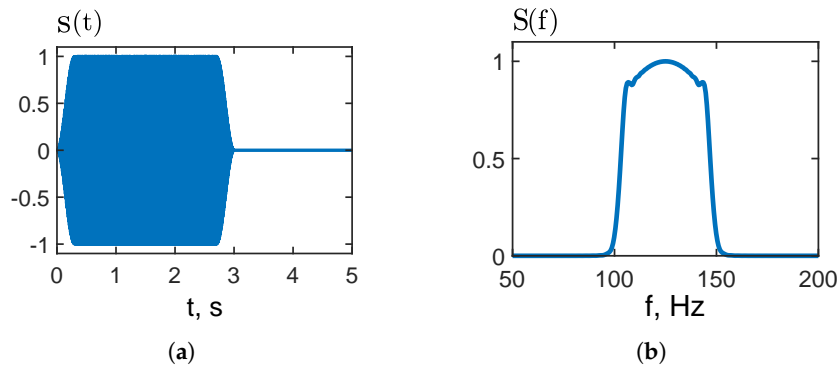


Figure 2. Source LFM signal: (a) signal time dependence $s(t)$; (b) signal spectrum $S(f)$.

Figure 2 illustrates the LFM signal used in the study. Figure 2(a) shows the time-domain waveform $s(t)$. The signal has a unit amplitude and a finite duration of $\tau = 3$ s; outside this interval, the signal is (approximately) zero. To reduce spectral smearing, smooth rise and fall segments are applied at the beginning and end. The instantaneous frequency linearly increases from $f_1 = 100$ Hz at $t = 0$ to $f_2 = 150$ Hz at $t = \tau = 3$ s, i.e., an up-chirp with slope $k = (f_2 - f_1)/\tau = 16.667$ Hz/s. Figure 2(b) presents the normalized magnitude spectrum $|S(f)|$. The energy is concentrated within the passband of 100–150 Hz (bandwidth of $\Delta f = 50$ Hz, center frequency of $f_0 \approx 125$ Hz), producing a nearly flat-top profile within the band and a rapid roll-off outside it.

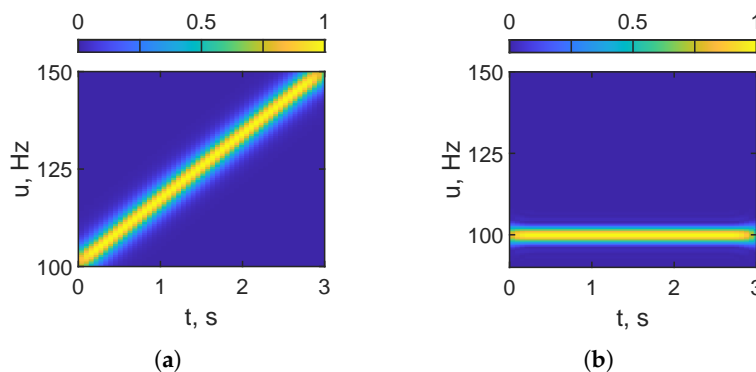


Figure 3. STFrFT of LFM source signal: (a) $S(t, u)$ – STFrFT of $s(t)$, parameter value is $p = 1$; (b) $S(t, u)$ – STFrFT of $s(t)$, parameter value is $p = 0.994$.

Figure 3 visualizes the STFrFT of the LFM source signal. Figure 3(a) corresponds to order $p = 1$ (i.e., the conventional STFT). The energy forms an oblique ridge that tracks the linear sweep $f(t) = f_1 + kt$ from 100–150 Hz over 0–3 s, with $k = 16.667$ Hz/s. Figure 3(b) uses an order matched to the chirp rate, $p = 0.994$; the representation is effectively de-chirped, and the energy collapses into a nearly horizontal ridge, indicating the transformed signal's near time-invariance. In both panels, the vertical axis is frequency (Hz), the horizontal axis is time (s), and the color scale shows the normalized magnitude (from 0 to 1). In the STFrFT, the order p sets the rotation angle $\alpha = p\pi/2$ of the time-frequency plane. Optimal de-chirping occurs when the rotation compensates for the chirp slope in the (t, u) plane: which is represented by the equation $\alpha = \arctan(2\pi k)$, $p = \frac{2}{\pi} \alpha$. With $f_1 = 100$ Hz, $f_2 = 150$ Hz, and $\tau = 3$ s, we obtain $k = 16.667$ Hz/s, $\alpha \approx 1.561$ rad, and $p \approx 0.994$. For a down-chirp ($k < 0$), the optimal angle flips sign ($\alpha \rightarrow -\alpha$), so the optimal order becomes $-p$. In practice, the horizontal orientation of the STFrFT $S(t, u)$ Figure 3(b) yields higher energy concentration and substantially increases the signal-to-noise ratio (SNR) of the received signal.

3.2. Shallow Water Waveguide and Transfer Function

Consider the canonical shallow-water waveguide. The waveguide consists of a shallow, horizontally homogeneous water layer of constant depth over a flat seabed. This model is widely used in underwater acoustics because it provides a simplified yet rigorous context for isolating the influence of individual environmental parameters.

The parameters used in the numerical simulation of the shallow-water waveguide are listed in Table 2.

Table 2. Shallow water waveguide parameters.

Parameter	$\Delta f = 100\text{--}150\text{ Hz}$
1. Waveguide depth H	50 m
2. Water sound speed	1500 m/s
3. Bottom refractive index	$n_b = 0.84 (1 + i 0.03)$
4. Bottom density	$\rho_b = 1.8\text{ g/cm}^3$
5. Modes count	$M = 3$
6. Receiver coordinates	$r_q = 0, z_q = 45\text{ m}$
7. Source coordinates	$r_s = 10\text{ km}, z_s = 15\text{ m}$

Calculations were performed for the frequency band of $\Delta f = 100\text{--}150\text{ Hz}$. The waveguide has a depth of $H = 50\text{ m}$ and a water sound speed of $c = 1500\text{ m s}^{-1}$. The seabed is modeled with a complex refractive index of $n_b = 0.84 (1 + i 0.03)$ and a density $\rho_b = 1.8\text{ g cm}^{-3}$. The receiver is placed at a range of $r_q = 0$ and a depth of $z_q = 45\text{ m}$, while the source is located at $r_s = 10\text{ km}$ and a depth of $z_s = 15\text{ m}$.

The sound field is represented by $M = 3$ normal modes. The values of the propagation constants are $h_m(\omega_0)$ and group velocities $u_m(\omega_0) = 1 / (\frac{dh_m(\omega_0)}{d\omega})$, $\omega = 2\pi f$, for the considered shallow water waveguide with the depth of $H = 50\text{ m}$ are given in Table 3. As can be seen, $h_m(\omega_0) \sim 0.49\text{--}0.52\text{ m}^{-1}$ and $\frac{dh_m(\omega_0)}{d\omega} \sim 6.7 \cdot 10^{-4} \text{--} 7.0 \cdot 10^{-4} (\text{m/s})^{-1}$.

Table 3. Sound field mode parameters ($f = 110\text{ Hz}$).

m -th mode	$(dh_m/d\omega) \cdot 10^4, (\text{m/s})^{-1}$	h_m, m^{-1}
1	6.7015	0.474323
2	6.8212	0.464355
3	7.0596	0.446709

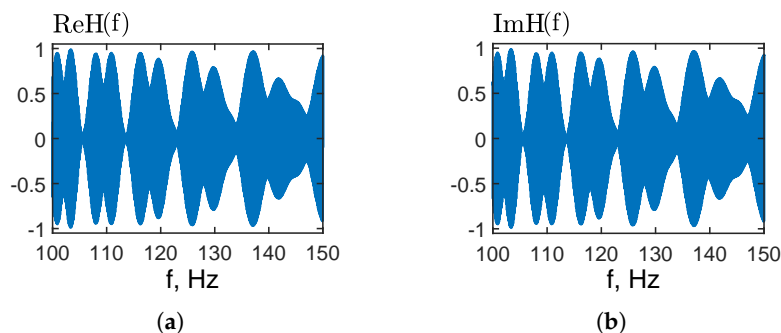


Figure 4. Shallow water waveguide transfer function $H(f)$: (a) real part of transfer function $\text{Re } H(f)$; (b) imaginary part of transfer function $\text{Im } H(f)$.

Figure 4 shows the complex transfer function $H(f)$ of the shallow water waveguide across the 100–150 Hz band. Figure 4(a) shows the real part, $\text{Re } H(f)$. Figure 4(b) illustrates the imaginary part, $\text{Im } H(f)$. Both components exhibit pronounced quasi-periodic oscillations with frequent zero crossings,

which are characteristic of modes interference in shallow water. The real and imaginary parts of $H(f)$ have comparable magnitudes (normalized to unity), indicating a strongly frequency-dependent phase response over the considered frequency band.

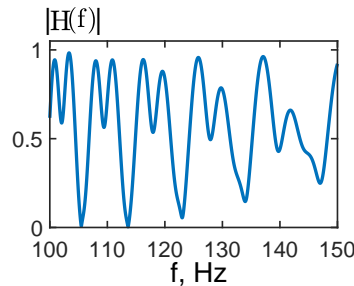


Figure 5. Shallow water waveguide transfer function $H(f)$: absolute value $|H(f)|$.

Figure 5 presents the magnitude of the shallow-water waveguide transfer function, $|H(f)|$, over the 100–150 Hz band. The normalized curve (0–1) and shows pronounced variability with alternating peaks and deep notches, reflecting constructive and destructive modal interference in the waveguide. Unlike the LFM signal at the source, the shallow-water waveguide transfer function exhibits substantial frequency dependence within the 100–150 Hz band, as seen in the figure. This, in turn, modifies the spectral (frequency) structure of the LFM source signal at the receiver after propagation through the shallow-water waveguide. We will examine this structure in the next section.

3.3. Receiver LFM Signal

This simulation considers the received LFM signal in the presence of noise. The received signal spectrum $S_r(\omega)$ is modeled as the product of the LFM source spectrum $S_s(\omega)$ and the shallow water waveguide transfer function $H(\omega)$, plus a realization of the noise spectrum realization in the frequency domain $N(\omega)$:

$$S_r(\omega) = S_s(\omega) H(\omega) + N(\omega). \quad (35)$$

Equation (35) shows that the observed spectrum is the source spectrum modulated by the frequency-dependent characteristics of the shallow water waveguide $H(\omega)$.

Figure 6 presents the received LFM signal with the parameters given in Table 1 in a shallow water waveguide with the parameters in Tables 2 and 3. Figure 6(a) shows the time domain of the receiver LFM signal $s(t)$: a finite-duration, amplitude-tapered chirp that occupies approximately the first 3 s of the record and is followed by silence. The instantaneous frequency increases with time, consistent with an up-chirp. Figure 6(b) displays the magnitude spectrum $|S(f)|$ computed from $s(t)$. The signal energy is concentrated in the 100–150 Hz band, which corresponding to the band-limiting of the LFM source signal. Unlike the source signal, the spectrum of the received LFM signal is characterized by pronounced variability with alternating peaks and deep notches, resulting from constructive and destructive modal interference in the shallow water waveguide.

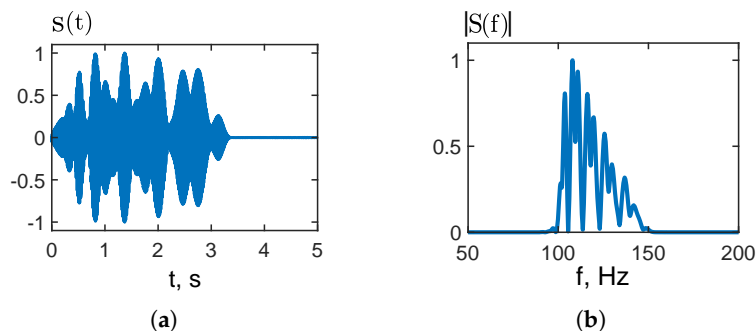


Figure 6. Receiver LFM signal: (a) signal time dependence $s(t)$; (b) signal spectrum $S(f)$. Noise is absent.

Figure 7 illustrates the STFrFT of the received LFM waveform $s(t)$ for two fractional orders in the noise-free case. Figure 7(a), with $p = 1$ (i.e., the conventional STFT), shows the characteristic up-chirp as a bright ridge rising from about 100 to 150 Hz over 0–3 s. In contrast, Figure 7(b) with $p = 0.994$ ($\alpha \approx 1.561$ rad) effectively rotates the time-frequency representation: the chirp is nearly flattened and its energy is concentrated in a narrow, almost horizontal band near 100 Hz. Though the received LFM signal is characterized by pronounced variability with alternating peaks and deep notches due to constructive and destructive modal interference, Figure 7 demonstrates the usefulness of the STFrFT for de-chirping the received LFM signal in a shallow-water waveguide.

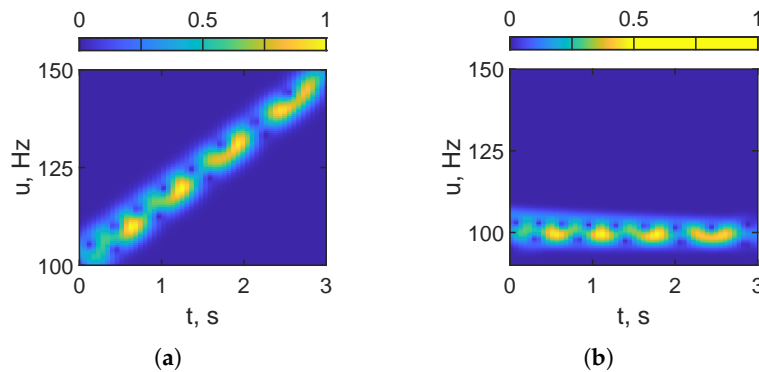


Figure 7. STFrFT of receiver LFM signal: (a) $S(t, u)$ – STFrFT of $s(t)$, parameter value is $p = 1$; (b) $S(t, u)$ – STFrFT of $s(t)$, parameter value is $p = 0.994$. Noise is absent.

Figure 8 shows the short-time fractional Fourier transform (STFrFT) of the noisy received LFM waveform $s(t)$ at $\text{SNR} = -30$ dB. Figure 8(a), with $p = 1$ (the conventional STFT), is dominated by diffuse noise and the up-chirp is not discernible. Figure 8(b) with $p = 0.994$, effectively de-chirps the waveform and concentrates its energy into a narrow, nearly horizontal band near 100 Hz by selecting a fractional order close to the LFM signal’s chirp rate. This makes it possible to effectively filter the received LFM signal from the noise. The result of this filtering is presented in the next figure.

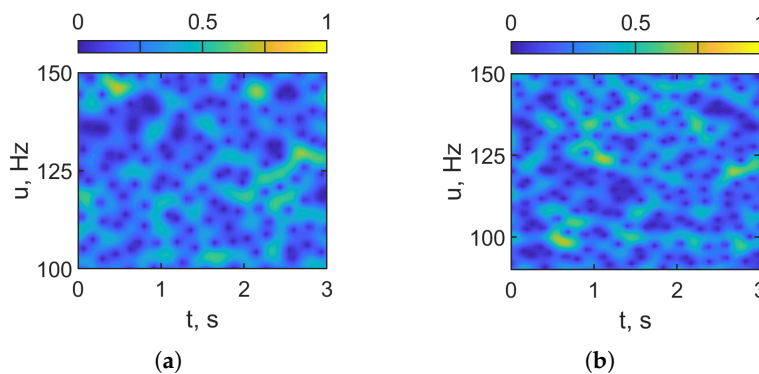


Figure 8. STFrFT of receiver LFM noisy signal after denoising. (a) $S(t, u)$ – STFrFT of $s(t)$, parameter value is $p = 1$; (b) $S(t, u)$ – STFrFT of $s(t)$, parameter value is $p = 0.994$. $\text{SNR} = -30$ dB.

Figure 9 shows the result of noise filtering in the STFrFT domain for the noisy received LFM signal with an input of $\text{SNR} = -30$ dB. The received LFM signal is filtered in the STFrFT domain, as shown in Figure 9(a), with an order matched to the chirp parameter ($p = 0.994$). In this case, the signal representation is effectively de-chirped, that is, the energy collapses into a narrow, nearly horizontal band near 100 Hz. This ensures high filtering effectiveness. After filtering the LFM signal, the inverse STFrFT ($p = 0.994$) is applied. Then, the forward STFrFT ($p = 1$) is then applied to the denoised signal. Figure 9(b) shows that, using the conventional STFT ($p = 1$), the energy of the denoised received LFM signal aligns with the expected LFM trajectory. This forms an ascending ridge from approximately 100

to 150 Hz over 0–3 s. Consequently, we obtain the spectral distribution (STFT) of the noise-suppressed LFM signal, which can be used to construct the source interferogram and hologram.

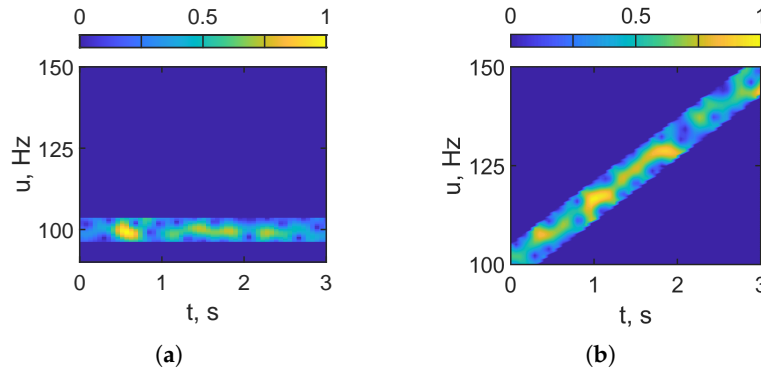


Figure 9. STFrFT of receiver LFM noisy signal: (a) $S(t, u)$ – STFrFT of $s(t)$, parameter value is $p = 0.994$; (b) $S(t, u)$ – STFrFT of $s(t)$, parameter value is $p = 1$. SNR = −30 dB.

Compared to the noisy case, denoising significantly reduces the spectral noise floor and reveals the signal structure. This improves chirp-parameter estimation accuracy and enables more effective Fourier transform (FT)-based holographic processing of low-signal-to-noise ratio (SNR) LFM signals. The following sections examine the effectiveness of this FrFT-based holographic processing for LFM signals at low SNR.

3.4. Interferogram and Hologram of Non-Moving LFM Source ($v = 0$ m/s)

This section reports on the results of holographic processing obtained from numerical simulations for a stationary LFM source, $v = 0$ m/s, in a shallow-water waveguide. The LFM waveform parameters used in the simulations are listed in Table 1, and the shallow water waveguide parameters are compiled in Table 2.

Simulation geometry. The source was placed at $(r_s, z_s) = (10 \text{ km}, 15 \text{ m})$, the receiver was located at $(r_q, z_q) = (0, 45 \text{ m})$. Thus, the horizontal separation remained fixed at $r_0 = 10 \text{ km}$. The numerical simulation model is shown in Figure 10.

Holographic Signal Processing Settings. The analysis was confined to the frequency band $f = 100$ –120 Hz. The total observation interval was $\Delta t = 300$ s; individual realizations had a duration $T = 5$ s with a hop of $\delta T = 4$ s between consecutive segments. A modal representation with $M = 3$ modes was employed. The corresponding propagation constants $h_m(\omega_0)$ and group velocities $u_m(\omega_0) = (dh_m(\omega_0)/d\omega)^{-1}$ are reported in Table 3.

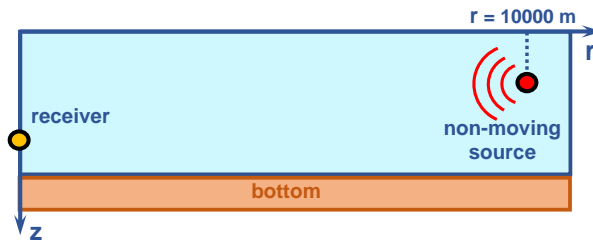


Figure 10. Numerical simulation model. LFM source signal. Non-moving source: ($v = 0$ m/s).

Figure 11 presents the results of the holographic signal processing for a stationary LFM signal source in a shallow water waveguide. No noise is present. Figure 6(a) shows the interferogram $I(f, t)$, where the spectral content in the 100–120 Hz band remains stable throughout the observation interval, reflecting the absence of variations due to source motion. Figure 11(b) displays the hologram $F(\tau, \tilde{v})$. As can be seen, the focal spots in the hologram domain for a stationary source are located along the τ -axis.

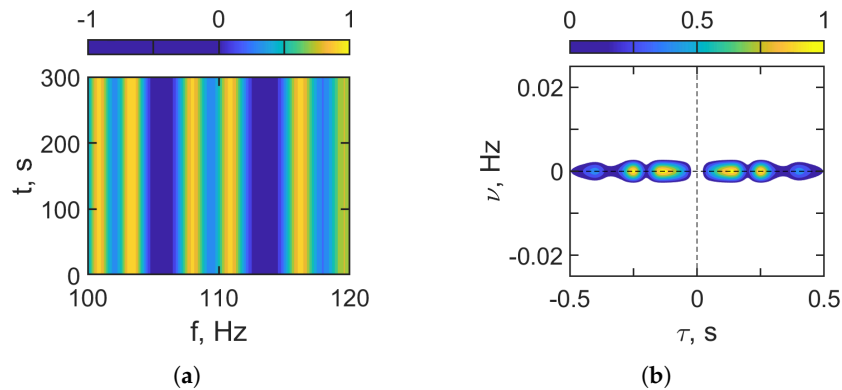


Figure 11. Receiver LFM signal. (a) Distribution $I(f, t)$ in interferogram domain. (b) Distribution $F(\tau, \tilde{\nu})$ in hologram domain. Frequency band: $\Delta f = 100\text{--}120$ Hz. Non-moving source: $v = 0$ m/s. Noise is absent.

Table 4. Source of LFM signal parameters estimation. Non-moving source. Noise is absent.

No.	$\Delta f = 100\text{--}120$ Hz
1.	$\delta f / \delta t \approx -0.0 \text{ s}^{-2}$
2.	$\tau_1 = 1.25 \cdot 10^{-1} \text{ s}$
3.	$\nu_1 = 0.0 \cdot 10^{-3} \text{ Hz}$
4.	$\dot{v} = 0.0 \text{ m/s}$
5.	$\dot{r}_0 = 10.43 \text{ km}$

Table 4 compiles the holographic signal processing results for the frequency band $\Delta f = 100\text{--}120$ Hz. As Figure 11 shows, the interferogram exhibits essentially no frequency drift, $\delta f / \delta t \approx 0.0 \text{ s}^{-2}$. In the hologram domain, the dominant focal spot is located at $\tau_1 = 0.125 \cdot 10^{-1} \text{ s}$ and $\nu_1 = 0.0 \cdot 10^{-3} \text{ Hz}$, consistent with a stationary source. Inverting the holographic parameters yields the following source estimates $\dot{v} = 0.0 \text{ m/s}$ and $\dot{r}_0 = 10.43 \text{ km}$. The corresponding errors are 0 % for the velocity and 4.3 % for the range.

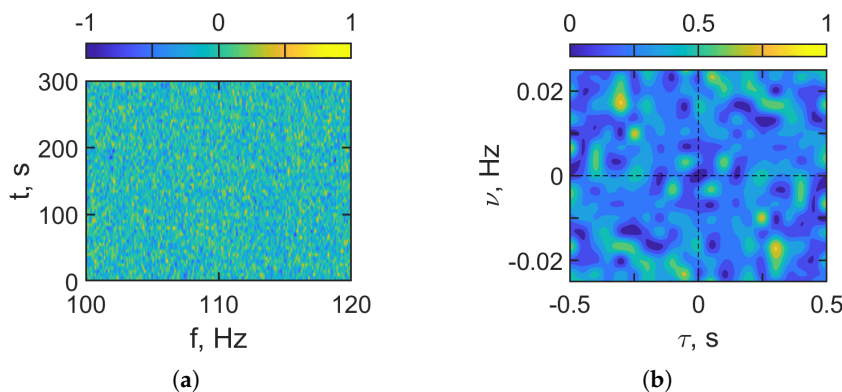


Figure 12. Receiver LFM noisy signal. Conventional HSP. (a) Distribution $I(f, t)$ in interferogram domain. (b) Distribution $F(\tau, \tilde{\nu})$ in hologram domain. Frequency band: $\Delta f = 100\text{--}120$ Hz. Non-moving source: $v = 0$ m/s. Noise is present. SNR = -30 dB.

Figure 12 presents the conventional HSP outputs for the noisy received LFM signal in the band $\Delta f = 100\text{--}120$ Hz for a stationary source ($v = 0$) at SNR = -30 dB. Figure 12(a) shows the interferogram $I(f, t)$. Without FrFT-based filtering of the receiver LFM signal, the Figure 12(a) is dominated by broadband noise. The quasi-periodic vertical interference fringes observed in the noise-free case are no longer discernible. No persistent time-frequency structure can be reliably identified. Figure 12(b) shows the hologram $F(\tau, \nu)$. For a stationary source the focal spots should lie along the abscissa

($\nu = 0$). However, the high noise level in Figure 12(b) largely masks the focal spots, distributed across the hologram domain. Clearly, the noisy hologram in panel (b) does not allow for reliable estimation of the coordinates of the LFM source's focal spots or reconstruction of its parameters. These results underscore the need for FrFT-domain denoising prior to holographic signal processing under low-SNR conditions ($\text{SNR} \leq -30$ dB).

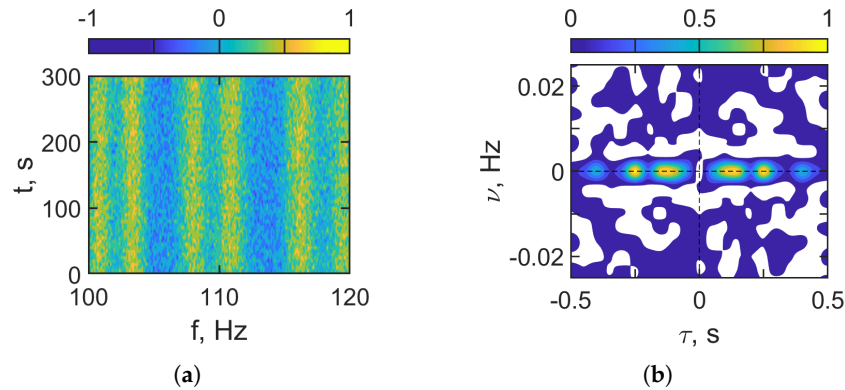


Figure 13. Receiver LFM noisy signal after denoising. HSP based on FrFT. (a) Distribution $I(f, t)$ in interferogram domain. (b) Distribution $F(\tau, \tilde{\nu})$ in hologram domain. Frequency band: $\Delta f = 100\text{--}120$ Hz. Non-moving source: $v = 0$ m/s. Noise is present. $\text{SNR} = -30$ dB.

Figure 13 presents the results of holographic signal processing for the noisy received LFM signal after FrFT-based denoising ($\Delta f = 100\text{--}120$ Hz, $v = 0$ m/s, $\text{SNR} = -30$ dB). Using the FrFT filter significantly improves the outcome of the holographic processing. In the interferogram domain (Figure 13(a)), the time-frequency structure is clearer, with pronounced vertical, quasi-periodic interference fringes now visible. In the hologram domain (Figure 13(b)), the focal spots associated with a stationary source are sharply localized along the $\nu = 0$ axis. This enhancement enables the reliable determination of the focal-spot coordinates and, consequently, the accurate estimation of the source parameters.

Table 5. Source of LFM signal parameters estimation. Non-moving source. Noise is present.

No.	$\Delta f = 100\text{--}120$ Hz
1.	$\delta f / \delta t \approx -0.0 \text{ s}^{-2}$
2.	$\tau_1 = 1.27 \cdot 10^{-1} \text{ s}$
3.	$\nu_1 = 0.0 \cdot 10^{-3} \text{ Hz}$
4.	$\dot{v} = 0.0 \text{ m/s}$
5.	$\dot{r}_0 = 10.61 \text{ km}$

Table 5 compiles the holographic signal processing results for a stationary source in the presence of noise across the band $\Delta f = 100\text{--}120$ Hz. The interferogram shows essentially no frequency drift in the noisy case (see Figure 13), with a value of approximately $\delta f / \delta t \approx -0.0 \text{ s}^{-2}$. In the hologram domain, the dominant focal spot is located at $\tau_1 = 1.27 \cdot 10^{-1} \text{ s}$ and $\nu_1 = 0.0 \cdot 10^{-3} \text{ Hz}$, consistent with a non-moving source. Inverting these holographic parameters yields the source estimates of $\dot{v} = 0.0 \text{ m/s}$ and $\dot{r}_0 = 10.61 \text{ km}$. These values are consistent with a stationary source. The range estimate remains close to the nominal value. The error in the reconstructed source values amounts to 0 % for the velocity and 6.1 % for the range. The presented results demonstrate the high effectiveness of FrFT-based denoising in holographic signal processing of an LFM signal from a stationary source in a shallow water waveguide under low SNR conditions ($\text{SNR} = -30$ dB).

3.5. Interferogram and Hologram of Moving LFM Source ($v = -3$ m/s)

This section presents the results of holographic processing obtained from numerical simulations for a moving LFM signal source with a velocity of $v = -3$ m/s, in a shallow water waveguide. The LFM signal parameters used in the simulations are listed in Table 1, and the shallow water parameters are compiled in Table 2.

Simulation geometry. The source was placed at $(r_s, z_s) = (10$ km, 15 m), and the receiver was located at $(r_q, z_q) = (0, 45$ m), so the horizontal separation remained fixed at $r_0 = 10$ km. The numerical simulation model is shown in Figure 14.

Holographic Signal Processing settings. The analysis was confined to the band $f = 100$ –120 Hz. The total observation interval was $\Delta t = 300$ s; individual realizations had a duration $T = 5$ s with a hop of $\delta T = 4$ s between consecutive segments. A modal representation with $M = 3$ modes was employed. The corresponding propagation constants $h_m(\omega_0)$ and group velocities $u_m(\omega_0) = (dh_m(\omega_0)/d\omega)^{-1}$ are reported in Table 3.

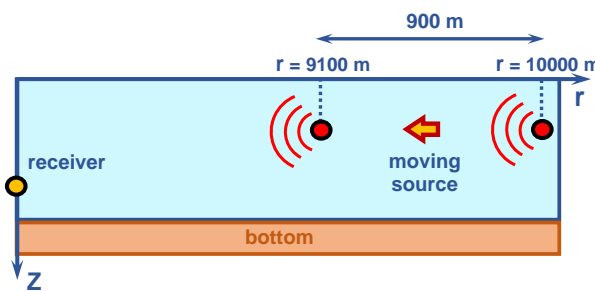


Figure 14. Numerical simulation model. LFM source signal. Moving source ($v = -3$ m/s).

Figure 15 shows the results of holographic signal processing for a moving LFM source in a shallow-water waveguide with a velocity of $v = -3$ m/s. There is no noise. Figure 15(a) shows the interferogram $I(f, t)$: pronounced oblique, quasi-periodic fringes with a non-zero slope $\delta f / \delta t \approx -0.037$, s^{-2} traverse the 100–120 Hz band over the observation interval, reflecting the induced frequency variation due to the source motion. Figure 15(b) displays the hologram $F(\tau, \nu)$. The focal spots are clearly resolved, displaced from the τ -axis and centered at $\nu \neq 0$, and appear approximately symmetric about $\tau = 0$ along an oblique locus in the (τ, ν) plane. The locations of these spots provide reliable coordinates of focal spots for estimating the source parameters (range and velocity), consistent with a moving source.

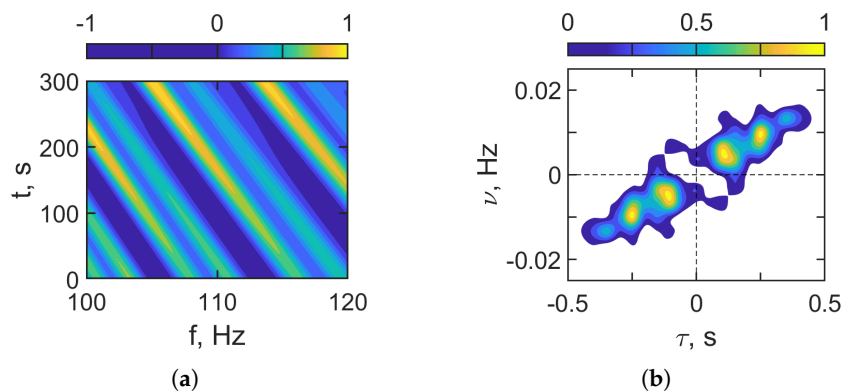


Figure 15. Receiver LFM signal. (a) Distribution $I(f, t)$ in interferogram domain. (b) Distribution $F(\tau, \tilde{\nu})$ in hologram domain. Frequency band: $\Delta f = 100$ –120 Hz. Moving source: $v = -3$ m/s. Noise is absent.

Table 6 summarizes the holographic signal processing results for a *moving* source in the band $\Delta f = 100$ –120 Hz (noise-free case). The interferogram indicates a non-zero frequency drift, $\delta f / \delta t \approx -0.037$ s^{-2} . In the hologram domain, the dominant focal spot is found at $\tau_1 = 1.21 \cdot 10^{-1}$ s and

$\nu_1 = 3.45 \cdot 10^{-3}$ Hz, which is consistent with a frequency shift due to source motion. Inverting these holographic parameters yields the source estimates $\dot{v} = -3.47$ m/s and $\dot{r}_0 = 10.1$ km. These values are consistent with a moving source and are close to the nominal settings. The corresponding errors are 15 % for the velocity and 1.0% for the range.

Table 6. Source of LFM signal parameters estimation. Moving source. Noise is absent.

No.	$\Delta f = 100\text{--}120$ Hz
1.	$\delta f / \delta t \approx -0.037 \text{ s}^{-2}$
2.	$\tau_1 = 1.21 \cdot 10^{-1} \text{ s}$
3.	$\nu_1 = 3.45 \cdot 10^{-3} \text{ Hz}$
4.	$\dot{v} = -3.47 \text{ m/s}$
5.	$\dot{r}_0 = 10.1 \text{ km}$

Figure 16 presents holographic signal processing results for the noisy received LFM signal without FrFT-based denoising ($\Delta f = 100\text{--}120$ Hz, $v = -3$ m/s, SNR = -30 dB). Omitting the FrFT filter markedly degrades the outcome of the holographic processing. In the interferogram domain (Figure 16(a)), the time–frequency structure is overwhelmed by broadband noise and the slanted, quasi-periodic interference fringes expected for a moving source are not visible. In the hologram domain (Figure 16(b)), the energy is diffuse and low-contrast. The focal spots cannot be localized. They are heavily masked by noise. The absence of a well-defined structure prevents determination of the focal-spot coordinates and, consequently, makes source parameters estimation impossible. These results underscore the need for FrFT-domain denoising prior to holographic signal processing under low-SNR conditions (SNR ≤ -30 dB).

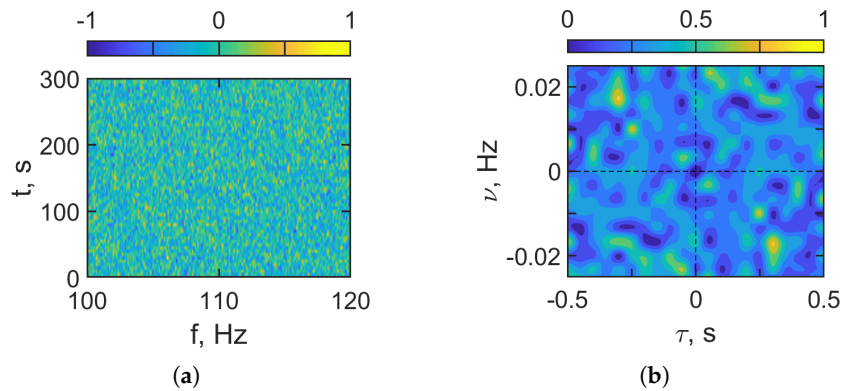


Figure 16. Receiver LFM signal. Conventional HSP. (a) Distribution $I(f, t)$ in interferogram domain. (b) Distribution $F(\tau, \tilde{\nu})$ in hologram domain. Frequency band: $\Delta f = 100\text{--}120$ Hz. Moving source: $v = -3$ m/s. Noise is present. SNR = -30 dB.

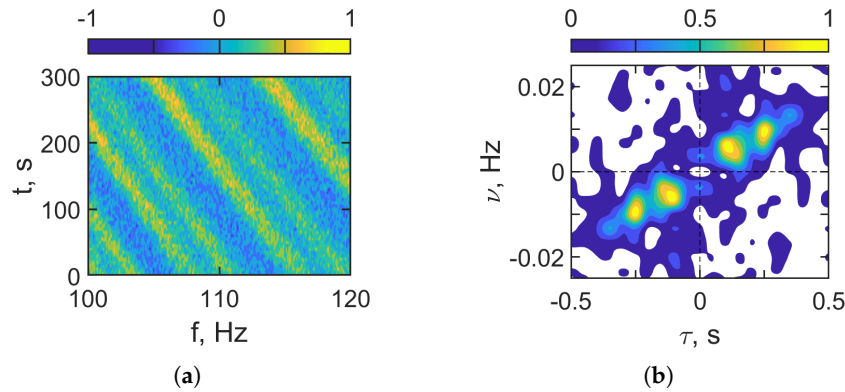


Figure 17. Receiver LFM signal. HSP based on FrFT. (a) Distribution $I(f, t)$ in interferogram domain. (b) Distribution $F(\tau, \tilde{\nu})$ in hologram domain. Frequency band: $\Delta f = 100\text{--}120$ Hz. Moving source: $v = -3$ m/s. Noise is present. SNR = -30 dB.

Figure 17 presents the results of holographic signal processing for the noisy received LFM signal after FrFT-based denoising ($\Delta f = 100\text{--}120$ Hz, $v = -3$ m/s, SNR = -30 dB). Applying the FrFT filter significantly improves the outcome of the holographic processing. In the interferogram domain (Figure 17(a)), the time-frequency structure is clear: slanted, quasi-periodic interference fringes with a non-zero slope $\delta f / \delta t$ are visible across the band, which is consistent with Doppler variation from the moving source. In the hologram domain (Figure 17(b)), energy collapses into compact focal spots displaced from the $\nu = 0$ axis. This enhancement enables the reliable determination of the focal-spot coordinates and, consequently, accurate estimation of the source parameters (velocity and range) under low-SNR shallow-water conditions.

Table 7. Source of LFM signal parameters estimation. Moving source. Noise is present.

No.	$\Delta f = 100\text{--}120$ Hz
1.	$\delta f / \delta t \approx -0.036 \text{ s}^{-2}$
2.	$\tau_1 = 1.15 \cdot 10^{-1} \text{ s}$
3.	$\nu_1 = 3.81 \cdot 10^{-3} \text{ Hz}$
4.	$\dot{v} = -3.82 \text{ m/s}$
5.	$\dot{r}_0 = 9.6 \text{ km}$

Table 7 summarizes the holographic signal processing results for a *moving* source in the band $\Delta f = 100\text{--}120$ Hz with noise present. The interferogram shows a non-zero frequency drift, $\delta f / \delta t \approx -0.036 \text{ s}^{-2}$. In the hologram domain, the dominant focal spot is located at $\tau_1 = 1.15 \cdot 10^{-1} \text{ s}$ and $\nu_1 = 3.81 \cdot 10^{-3} \text{ Hz}$, which is consistent with a nonzero Doppler shift. Inverting these holographic parameters yields the following source estimates $\dot{v} = -3.82 \text{ m/s}$ and $\dot{r}_0 = 9.6 \text{ km}$. These values are consistent with a moving source. Compared with the nominal settings ($v = -3 \text{ m/s}$, $r_0 = 10 \text{ km}$), the errors are about 27.3 % in velocity and 4% in range.

These results demonstrate that incorporating FrFT-based denoising as a preprocessing step in holographic signal processing is highly effective for LFM signals from a stationary source in a shallow-water waveguide under very low SNR. At (SNR = -30 dB), the method markedly lowers the spectral noise floor, restores the interferometric structure, and produces well-localized focal spots in the hologram. This improves detectability, as well as the accuracy and stability of subsequent parameter estimates (e.g., range) compared to conventional processing.

4. Conclusions

The paper proposes a FrFT-based holographic signal processing method for an LFM signal of a moving source in shallow water waveguide. The study demonstrates that applying the short-time fractional Fourier transform for the formation and analysis of holograms of a moving LFM source

provides reliable estimations of the source parameters even under high noise levels. Under strong noise conditions: (i) rotating the FrFT representation in the time-frequency domain concentrates the energy of the LFM chirp in the frequency domain, (ii) denoising the compacted energy, and (iii) then performing quasi-coherent interferometric accumulation is performed by means of a two-dimensional Fourier transform to form a noise-free source hologram. The resulting source hologram's structure is similar to that of a source hologram in the absence of noise. The focal spots of the source hologram align along a straight line passing through the origin. The coordinates of the hologram's focal spot are determined by the source parameters (range and radial velocity). Thus, the proposed FrFT-based holographic processing method can estimate the parameters of an LFM source even under strong noise conditions: $\text{SNR} \leq -30$ dB.

Key findings of paper.

- **Noise robustness and denoising.** Holographic signal processing based on the short-time fractional Fourier transform for the LFM signal of a stationary or moving source concentrates the energy into a nearly horizontal ridge. This enables effective denoising at input SNRs down to -30 dB and restores a clear holographic structure where conventional short-time Fourier transform processing fails.
- **Accuracy of parameter estimation (stationary source).** Quantitative analysis shows that the range of a stationary source can be recovered with an error of at most 10 %. In the noise-free case, the velocity and range errors are 0 % and 4 %; at $\text{SNR} = -30$ dB, the errors are 0 % and 6 %, respectively.
- **Accuracy of parameters estimation (moving source).** A quantitative analysis indicates that the range of a moving source can be recovered with an error of up to 5 %, whereas its velocity may incur errors of up to 30 %. In the noise-free case, the velocity and range errors are 15 % and 1 %, respectively; at $\text{SNR} = -30$ dB, these errors increase to 27 % and 4 %.
- **Effectiveness of the FrFT-based HSP method.** Comparing stationary and moving source types reveals that high noise levels cause only a minor increase in estimation errors relative to the noise-free case. These results confirm the robustness of the FrFT-based holographic signal processing method and its ability to deliver reliable results in realistic shallow-water conditions with high-noise levels.

FrFT-based holographic signal processing preserves the interpretability of holographic features while substantially improving the detectability of low-SNR LFM signal sources. Practical applications include estimating the range and velocity of a source in shallow water with a single receiver and easily integrating with existing holographic signal processing.

These findings expand the application of holographic techniques in underwater acoustics, demonstrating their effectiveness in noisy real-world settings. In particular, FrFT-based holographic processing of LFM signals yields stable, near-truth estimates of source parameters. This underscores the value of FrFT-based holographic processing for fundamental studies and operational ocean monitoring and surveillance in high-noise environments.

5. Future Works

The next phase of our research will focus on empirically validating the proposed FrFT-based holographic signal processing framework using legacy, well-instrumented, shallow-water experiments spanning diverse environments and source-receiver geometries – SWARM'95, Shallow Water 2006 (SW06), and ASIAEX 2001 ([61–65]). These campaigns encompass intense internal-wave fields, continental-shelf propagation, variable bathymetry and bottom types, and high noise levels — making them an ideal testing ground for noise-robust, single-receiver ranging and velocity estimation under complex conditions.

Author Contributions: Supervision and project administration, M.E. and S.P.; conceptualization and methodology, V.K. and S.P.; software, S.T., A.P., and N.L.; validation, M.E. and V.K.; formal analysis, M.E. and S.P.; writing –

original draft preparation, M.E. and S.P.; writing – review and editing, M.E. and S.P.; All authors have read and agreed to the published version of the manuscript.

Funding: This work was supported by grant from the Russian Science Foundation № 23-61-10024, <https://rscf.ru/project/23-61-10024/>.

Data Availability Statement: The original data used in the study are openly available. The waveguide model used in the simulation is based on parameters from the SWARM'95, SHALLOW WATER 2006, ASIEX 2001 experiments: [61–65].

Conflicts of Interest: The authors declare no conflicts of interest.

Abbreviations

The following abbreviations are used in this manuscript:

ISP	interferometric signal processing;
HSP	holographic signal processing;
FT	Fourier transform;
STFT	short-time Fourier transform;
FrFT	fractional Fourier transform;
STFrFT	short-time fractional Fourier transform;
LFM	linear frequency modulation;
2D	two-dimensional;
1D-FT	one-dimensional Fourier transform;
2D-FT	two-dimensional Fourier transform.

References

- Namias V. The fractional order Fourier transform and its application to quantum mechanics. *IMA Journal of Applied Mathematics*. 25(3):241-265. **1980**
- McBride A. C., Kerr F. H. On Namias' fractional Fourier transform. *IMA Journal of Applied Mathematics*. 39(2):159-175. **1987**
- Almeida L. B. The fractional Fourier transform and time-frequency representations. *IEEE Transactions on Signal Processing*. 42(11):3084-3091. **1994**
- Sejdić E., Djurović I., Stanković J. Fractional Fourier transform as a signal processing tool: An overview of recent developments. *Signal Processing*. 91(6):1351-1369. **2011**
- Su W., Tao R., Deng B. Discrete fractional Fourier transform: algorithms and applications in signal processing. *Signal Processing*. 156:44-63. **2019**.
- Lu Y. An effective representation for multi-component nonstationary signals based on the fractional Fourier transform. *Mechanical Systems and Signal Processing*. 178(10):109305. **2022**.
- Duhamel P., Vetterli M. Fast Fourier Transforms: A Tutorial Review and a State of the Art. *Signal Processing*. 19(1):17-34. **1990**
- Ozaktas H. M., Mendlovic D. Fourier transforms of fractional order and their optical interpretation. *Optics Communications*. 101:163-169. **1993**
- Ozaktas H. M., Mendlovic D. Fractional Fourier optics. *Journal of the Optical Society of America A*. 12(4):743-751. **1995**
- Tao R., Xin Y., Wang Y. Double image encryption based on random phase encoding in the fractional Fourier domain. *Optics Express*. 15:16067-16079. **2007**
- Tao R., Lang J., Wang Y. Optical image encryption based on the multiple-parameter fractional Fourier transform. *Optics Letters*. 33(6):581-583. **2008**
- Capus C., Brown K. E. Short-time fractional Fourier methods for the time-frequency representation of chirp signals. *Journal of the Acoustical Society of America*. 113(6):3253-3263. **2003**
- Locke J., White P. R. The performance of methods based on the fractional Fourier transform for detecting marine mammal vocalizations. *Journal of the Acoustical Society of America*. 130(4):1974-1984. **2011**
- Ozaktas H. M., Aytur O. Fractional Fourier domains. *Signal Processing*. 46:119-124. **1995**
- Xia X. G. On bandlimited signals with fractional Fourier transform. *IEEE Signal Processing Letters*. 3(3):72-74. **1996**

16. Erseghe T., Kraniuskas P., Cariolaro G. Unified fractional Fourier transform and sampling theorem. *IEEE Transactions on Signal Processing*. 47(12):3419-3423.**1999**
17. Ozaktas H. M., Barshan B., Mendlovic D., Onural L. Convolution, filtering, and multiplexing in fractional Fourier domains and their relation to chirp and wavelet transforms. *Journal of the Optical Society of America A*. 11(2):547-559.**1994**
18. Kutay M. A., Ozaktas H. M., Arikan O., Onural L. Optimal filtering in fractional Fourier domains. *IEEE Transactions on Signal Processing*. 45(5):1129-1143.**1997**
19. Qi L., Tao R., Zhou S. Y., Wang Y. Detection and parameter estimation of multicomponent LFM signal based on the fractional Fourier transform. *Science in China, Series F: Information Sciences*. 47:184-198.**2004**
20. Santhanam B., McClellan J. H. The discrete rotational Fourier transform. *IEEE Transactions on Signal Processing*. 44(4):994-998.**1996**
21. Ozaktas H. M., Arikan O., Kutay M. A., Bozdagi G. Digital computation of the fractional Fourier transform. *IEEE Transactions on Signal Processing*. 44(9):2141-2150.**1996**
22. Pei S. C., Yeh M. H., Tseng C. C. Discrete fractional Fourier transform based on orthogonal projections. *IEEE Transactions on Signal Processing*. 47(5):1335-1348.**1999**
23. Pei S. C., Ding J. J. Closed-form discrete fractional and affine Fourier transforms. *IEEE Transactions on Signal Processing*. 48(5):1338-1353.**2000**
24. Durak L., Arikan O. Short-time Fourier transform: Two fundamental properties and an optimal implementation. *IEEE Transactions on Signal Processing*. 51(5):1231-1242.**2003**
25. Zayed A. I. A convolution and product theorem for the fractional Fourier transform. *IEEE Signal Processing Letters*. 5(4):101-103.**1998**
26. Kraniuskas P., Cariolaro G., Erseghe T. Method for defining a class of fractional operations. *IEEE Transactions on Signal Processing*. 46(10):2804-2807.**1998**
27. Czerwinski R. N., Jones D. L. Adaptive Short-Time Fourier Analysis. *IEEE Transactions on Signal Processing*. 45(3):617-627.**1997**
28. Zhang Z., et al. Adaptive Short-Time Fourier Transform for Nonstationary Signal Analysis. *Mechanical Systems and Signal Processing*. 24(1):207-219.**2010**
29. Rybak J. Short-Time Fourier Transform Based on Metaprogramming. *Sensors*. 21(12):4123.**2021**
30. Sandoval S., Gerkmann T., Flandrin P. Recasting the (Synchrosqueezed) Short-Time Fourier Transform as Instantaneous Spectra. *IEEE Signal Processing Magazine*. 39(2):141-152.**2022**
31. Stankovic L., Alieva T., Bastiaans M. J. Time-frequency signal analysis based on the windowed fractional Fourier transform. *Signal Processing*. 83:2459-2468.**2003**
32. Katkovnik V. A new form of the Fourier transform for time-frequency estimation. *Signal Processing*. 47(2):187-200.**1995**
33. Djukanovic S., Dakovic M., Stankovic L. Local polynomial Fourier transform receiver for nonstationary interference excision in DSSS communications. *IEEE Transactions on Signal Processing*. 56(4):1627-1636.**2008**
34. Djurovic I. Robust adaptive local polynomial Fourier transform. *IEEE Signal Processing Letters*. 11(2):201-204.**2004**
35. Tao R., Li Y.-L., Wang Y. Short-time fractional Fourier transform and its applications. *IEEE Transactions on Signal Processing*. 58(5):2568-2580.**2010**
36. Weston D., Stevens K. Interference of wide-band sound in shallow water. *J. Sound Vib.* 21(1):57-64. **1972**.
37. Chuprov S. Interference structure of a sound field in a layered ocean. *Ocean Acoust., Curr. State*. 71-91. **1982**.
38. Ianniello J. Recent developments in sonar signal processing. *IEEE Signal Proc. Magazine*, 15(4):27-40. **1998**.
39. Thode A.M. Source ranging with minimal environmental information using a virtual receiver and waveguide invariant theory. *J. Acoust. Soc. Am.*, 108(4):1582-1594. **2000**.
40. Kuperman W.A., D'Spain G.L. Ocean acoustic interference phenomena and signal processing. *Ocean Acoust. Interfer. Phenom. Signal Proc.* 621 **2002**.
41. Rouseff D., Spindel R.C. Modeling the waveguide invariant as a distribution. *AIP Conf. Proc., Amer. Inst. Phys.* 621:137-150. **2002**.
42. Baggeroer A. B. Estimation of the distribution of the interference invariant with seismic streamers. *AIP Conf. Proc., Amer. Inst. Phys.* 621:151-170. **2002**.
43. Yang T. Beam intensity striations and applications. *J. Acoust. Soc. Am.*, 113(3):1342-1352. **2003**.
44. Heaney K. D. Rapid geoacoustic characterization using a surface ship of opportunity. *IEEE J. Oceanic Engrg.*, 29(1):88-99. **2004**.

45. Cockrell K. L., Schmidt H. Robust passive range estimation using the waveguide invariant. *J. Acoust. Soc. Am.*, 127(5):2780-2789. **2010**. 694
46. Rouseff D., Zurk L. M. Striation-based beam forming for estimating the waveguide invariant with passive sonar. *J. Acoust. Soc. Am. Express Lett.*, 130:76-81. **2011**. 695
47. Harrison C. H. The relation between the waveguide invariant, multipath impulse response, and ray cycles. *J. Acoust. Soc. Am.*, 129(5):2863-2877. **2011**. 696
48. Emmetiere R., Bonnel J., Gehant M., Cristol X., Chonavel T. Understanding deep-water striation patterns and predicting the waveguide invariant as a distribution depending on range and depth. *J. Acoust. Soc. Am.*, 143(6):3444-3454. **2018**. 697
49. Emmetiere R., Bonnel J., Cristol X., Gehant M., Chonavel T. Passive source depth discrimination in deep-water. *IEEE J. Select. Topics Signal Process.*, 13(1):185-197. **2019**. 698
50. Kuznetsov G. N., Kuzkin V. M., Pereselkov S. A. Spectrogram and localization of a sound source in a shallow sea. *Acoust. Phys.*, 63(4):449-461. **2017**. 699
51. Pereselkov S. A., Kuz'kin V. M. Interferometric processing of hydroacoustic signals for the purpose of source localization. *Journal of the Acoustical Society of America*. 151(2):666-676. **2022**. 700
52. Ehrhardt M., Pereselkov S. A., Kuz'kin V. M., Kaznacheev I., Rybyanets P. Experimental observation and theoretical analysis of the low-frequency source interferogram and hologram in shallow water. *J. Sound Vibr.* 544:117388. **2023**. 701
53. Pereselkov S., Kuz'kin V., Ehrhardt M., Tkachenko S., Rybyanets P., Ladykin N. Use of interference patterns to control sound field focusing in shallow water. *Journal of Marine Science and Engineering*. 11:559. **2023**. 702
54. Pereselkov S., Kuz'kin V., Ehrhardt M., Matvienko Y., Tkachenko S., Rybyanets P. The Formation of 2D Holograms of a Noise Source and Bearing Estimation by a Vector Scalar Receiver in the High-Frequency Band. *Journal of Marine Science and Engineering*. 12:704. **2024**. 703
55. Pereselkov S., Kuz'kin V., Ehrhardt M., Tkachenko S., Rybyanets, P., Ladykin, N. Three-Dimensional Modeling of Sound Field Holograms of a Moving Source in the Presence of Internal Waves Causing Horizontal Refraction. *J. Mar. Sci. Eng.* 11, 1922. **2023**. 704
56. Pereselkov S., Kuz'kin V., Ehrhardt M., Tkachenko S., Pereselkov A., Ladykin N. Influence of intense internal waves traveling along an acoustic path on source holographic reconstruction in shallow water. *Journal of Marine Science and Engineering*. 13:1409. **2025**. 705
57. Pereselkov S., Kuz'kin V., Ehrhardt M., Tkachenko S., Pereselkov A., Ladykin N. Effect of Irregular Bathymetry on Hologram Formation of a Moving Source in Shallow Water. *Preprint BUW-IMACM 25/12*, University of Wuppertal, August 2025. 706
58. Kuz'kin V. M., Pereselkov S. A. Holographic methods of hydroacoustic signals processing (review). *Akusticheskii Zhurnal (Acoustical Journal)*. 71(1):96-117. **2025**. 707
59. Hildebrand J. A., Frasier K. E., Baumann-Pickering S., Wiggins S. M. An empirical model for wind-generated ocean noise. *Journal of the Acoustical Society of America*. 149(6):4516-4533. **2021**. 708
60. Cho S., et al. Wind-dependent ambient noise level estimation in shallow coastal waters. *Continental Shelf Research*. 222:104398. **2021**. 709
61. Apel J. R., Badiy M., Chiu C.-S., Finette S., et al. An overview of the 1995 SWARM (Shallow-Water Acoustic Random Media) shallow-water internal-wave acoustic scattering experiment. *IEEE Journal of Oceanic Engineering*. 22(3):465-500. **1997**. 710
62. Tang D., Moum J. N., Lynch J. F., Abbot P., Chapman R., Dahl P. H., et al. Shallow Water '06: A joint acoustic propagation/nonlinear internal wave physics experiment. *Oceanography*. 20(4):156-167. **2007**. 711
63. Wei R.-C., Chen C.-F., Chan H.-C. Initial study of ambient noise modeling for the 2001 ASIAEX South China Sea experiment. *Journal of the Acoustical Society of America*. 115(5_Supplement):2508-2509. **2004**. 712
64. Lynch J. F., Ramp S. R., Dahl P. H., Chiu C.-S. Overview of results from the Asian Seas International Acoustics Experiment (ASIAEX) in the South China Sea 2001. *IEEE Journal of Oceanic Engineering*. 29(4):1067-1074. **2004**. 713
65. Headrick R. H., et al. Acoustic normal-mode fluctuation statistics in the 1995 SWARM internal-wave scattering experiment. *Journal of the Acoustical Society of America*. 107(1):201-220. **2000**. 714
66. Kohler W., Papanicolaou G. C. Wave propagation in a randomly inhomogeneous ocean. In: Keller JB Papadakis JS (Eds.), *Wave Propagation and Underwater Acoustics Lecture Notes in Physics, Springer*, 70:153-223. **1977**. 715
67. Jensen F. B., Kuperman W. A., Porter M. B., Schmidt H., Tolstoy A. *Computational Ocean Acoustics*. Springer. **2011**. 716
68. Brekhovskikh L. M., Lysanov Y. P. *Fundamentals of Ocean Acoustics*. Springer. **2013**. 717

Disclaimer/Publisher’s Note: The statements, opinions and data contained in all publications are solely those of the individual author(s) and contributor(s) and not of MDPI and/or the editor(s). MDPI and/or the editor(s) disclaim responsibility for any injury to people or property resulting from any ideas, methods, instructions or products referred to in the content.